ACS NANO

www.acsnano.org

ARTICLE

Sulfur Reduction Catalyst Design Inspired by Elemental Periodic Expansion Concept for Lithium–Sulfur Batteries

Yangyang Dong, Dong Cai,* Tingting Li, Shuo Yang, Xuemei Zhou, Yongjie Ge, Hao Tang, Huagui Nie, and Zhi Yang*

Cite This: *ACS Nano* 2022, 16, 6414–6425

Read Online

ACCESS | Metrics & More | Article Recommendations | Supporting Information

ABSTRACT: The key challenges facing the commercialization of lithium–sulfur (Li–S) batteries are shortening the lithium polysulfide (LiPS) intermediate existence time while accelerating solid-phase conversion reactions. Herein, inspired by highly efficient natural enzymes with Fe/N active sites for oxygen reduction reactions, we report a periodic expansion catalysis concept, i.e., Ru and P synergic stereoselectivity, for designing sulfur reduction reaction (SRR) catalysts. As a proof of concept, a RuP_2-configuration molecular catalyst was exploited to assemble an interlayer in Li–S batteries that adsorbs LiPSs, optimizes Li^+ migration paths, and catalyzes SRRs. Comprehensive investigation identified the elimination of steric hindrance and strong electron orbital couplings between metallic d band and nonmetallic p band as the main contributing factors of PEC for the SRRs. As a result, the Li–S battery with ~0.5 wt % catalyst additive showed enhanced cycling stability even under a high sulfur loading (6.5 mg cm^{-2}) and low electrolyte/sulfur ratio (9 μL mg^{-1}).

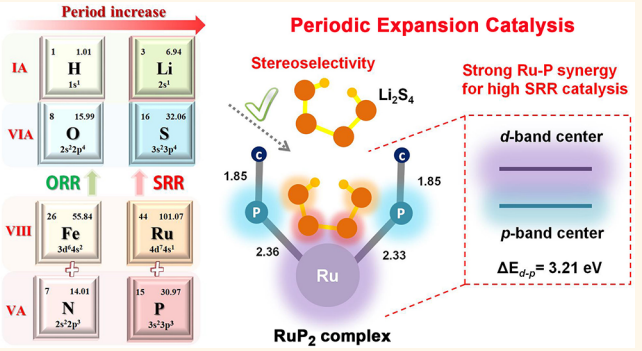

KEYWORDS: *lithium–sulfur batteries, lithium polysulfides, sulfur reduction reactions, periodic catalysis, d–p bands*

INTRODUCTION

The pursuit of a better future requires the adjustment of our energy supply structures. For example, new vehicles are increasingly abandoning traditional fossil fuels for battery-powered systems, where the desire for "green" batteries with a high energy density and long service life should be realized in an environmentally friendly manner. Sublimed sulfur is among the most promising candidates for this purpose owing to its environmentally benign nature, low cost, and high theoretical energy density.[1] When sulfur is paired with a lithium anode, the resulting lithium–sulfur (Li–S) full cell features a high theoretical energy density of 2600 Wh kg^{-1} and an extended lifetime.[2] However, the (electro)chemical reactions at sulfur cathodes involve multiphase polysulfide conversions with sluggish kinetics, resulting in low power and energy densities.[3,4] Furthermore, the diffusion of soluble lithium polysulfide (LiPS) intermediates through the electrolyte toward the Li anode results in a polysulfide shuttling effect, which destroys the quasi-equilibrium states, leading to rapid capacity decay and a shortened cycling lifetime.[5−7]

To tackle these issues, most studies to date have focused on confining sulfur within porous carbon[8] or other nanoarchitectures[9−11] with tailored surfaces and further introducing catalytic promoters to bind LiPSs/Li_2S and lower the energy barrier during reversible conversions of LiPSs and Li_2S. Although this approach is effective, the high weight percentages of conventional metal sulfides, carbides, oxides, nitrides, and vanadium catalysts sacrifice the overall energy density of Li–S batteries. Additionally, these less-efficient catalysts have only limited exposed surfaces to construct conductor/catalyst/electrolyte three-phase reactive interfaces. The resulting sluggish depletion of soluble LiPSs to Li_2S_2/Li_2S precipitates, accompanied by the rapid generation of LiPSs (S_8 → LiPSs), leads to LiPS accumulation in the electrolyte. This

Received: January 16, 2022
Accepted: April 5, 2022
Published: April 11, 2022

https://doi.org/10.1021/acsnano.2c00515
ACS Nano 2022, 16, 6414–6425

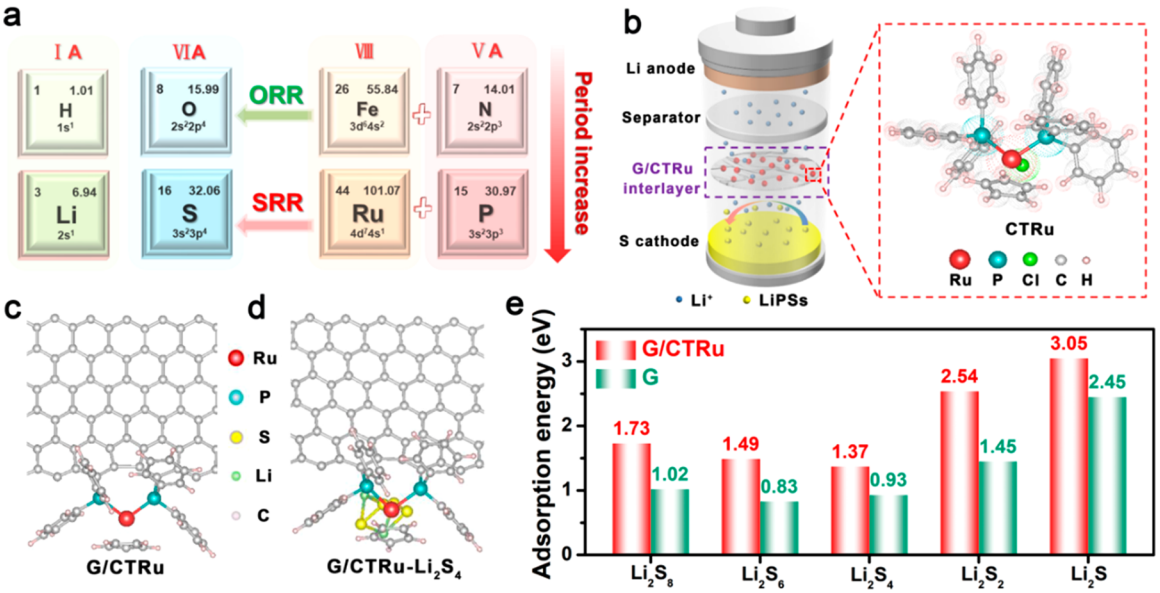

Figure 1. Inspiration and configuration of G/CTRu interlayers for advanced Li−S batteries. (a) Concept of our proposed periodic expansion catalysis concept from Fe/N activated ORR to Ru/P chemistry for SRR. (b) Schematic illustration of the CTRu molecule (right) and a Li−S battery model based on the G/CTRu interlayer (left). (c, d) Optimized geometric structures of the G/CTRu and G/CTRu-Li_2S_4 configurations, where the CTRu molecule is grafted onto the G film to block and catalyze LiPSs. The Ru, P, S, Li, and C atoms are presented by red, cyan, yellow, green, and light gray solid balls, respectively. (e) Binding energies of G/CTRu (red bar) and G (green bar) for Li_2S_8, Li_2S_6, Li_2S_4, Li_2S_2, and Li_2S based on DFT calculations.

causes large amounts of sulfur species to lose intimate contact with the electrode, which hinders electron/ion transport and potentially risks Li anode corrosion.[12,13] Accordingly, modulating sulfur reduction reactions (SRR), especially the conversion of LiPSs to Li_2S, which accounts for more than 75% of the total capacity, to rapidly decrease the LiPS concentration in the electrolyte has received research attention.[14−16] Therefore, designing highly efficient SRR catalysts and developing SRR concepts are important for improving Li−S battery performance.

Using nature to gain an understanding of fundamental scientific issues, such as the active structure, structure−activity relationships, and catalytic mechanisms of natural enzymes, might inspire the development of SRR catalysts or concepts in Li−S chemistry.[17,18] Some guidance is provided by the fuel cell field, where natural monooxygenase enzymes with Fe−N_4 active sites, such as cytochrome P450, have shown outstanding oxygen reduction reaction (ORR) kinetics.[19,20] In the periodic table of elements, H and O, as found in fuel cells, are located directly above Li and S, respectively, as found in Li−S batteries.[21−23] Therefore, by understanding the rules governing the element characteristics of congeners and motivated by the design of fuel cell catalysts (Fe/N → ORR),[24,25] the development of highly efficient SRR catalysts using elements positioned in the period below Fe and N, namely, Ru and P (Ru/P → SRR), might be beneficial (Figure 1a).[26−30] In addition, the steric resistance and stereoselectivity of catalysts, as other critical factors for mimicking natural enzymes, should also be considered to improve activities. Unlike the $2s^22p^4$ level of O, the valence electron orbital of S is $3s^23p^4$, which shows a larger radial electron cloud shell. To eliminate adverse effects of steric hindrance, Ru and P atoms with larger atomic radii may be favorable to enable electron couplings with S_8 molecules. Consequently, periodic expansion catalysis (PEC) has been used to derive a catalytic design concept.

In the present study, to take advantage of Ru/P synergy and verify this PEC concept in Li−S systems, we rationally designed and developed a highly efficient catalytic interlayer in Li−S batteries based on a substrate comprising chloro(cyclopentadienyl)bis(triphenylphosphine)ruthenium(II) (CTRu) and graphene (G), denoted as G/CTRu. Using in situ/ex situ spectroscopic analysis and density functional theoretical (DFT) simulations, G/CTRu was shown to optimize the migration paths of Li^+, reduce its transfer energy barrier, and accelerate the conversions of sulfur intermediates. Furthermore, various atomic substitution models were constructed to clarify the roles of Ru and P atoms in the synergistic effect on SRR. All intermediate states were also systematically studied. As a result, steric hindrance in the molecular structure and strong electron orbital couplings were proposed to play key roles in PEC, highlighting the regulation of electronic structures of metallic d-band centers by nonmetallic p bands. The G/CTRu interlayer clearly improved the electrochemical performance of Li−S batteries, delivering a high initial discharge capacity of 1460 mAh g^{-1} at 0.2 C (1 C = 1675 mA g^{-1}) and retaining ~588 mAh g^{-1} at 1 C after 500 cycles. Even under harsh conditions with a sulfur areal loading of 6.5 mg cm^{-2} and electrolyte/sulfur (E/S) ratio of 9 μL mg^{-1}, the cell still showed a specific capacity of 698 mAh g^{-1} after 120 cycles at 0.1 C, with a decay rate of 0.13%. This study provides a universal strategy for designing SRR molecular catalysts and tailoring their catalytic activity to improve the inherently sluggish kinetics of Li−S batteries.

RESULTS AND DISCUSSION

Structure, Configuration, and Strong LiPS Interaction of CTRu and the G/CTRu Interlayer in Li−S Batteries. Figure 1b shows the schematic configuration of the G/CTRu interlayer in Li−S batteries, where CTRu was composed of a central Ru(II) atom and coupled cyclopentadienyl (Cp) ring

https://doi.org/10.1021/acsnano.2c00515
ACS Nano 2022, 16, 6414−6425

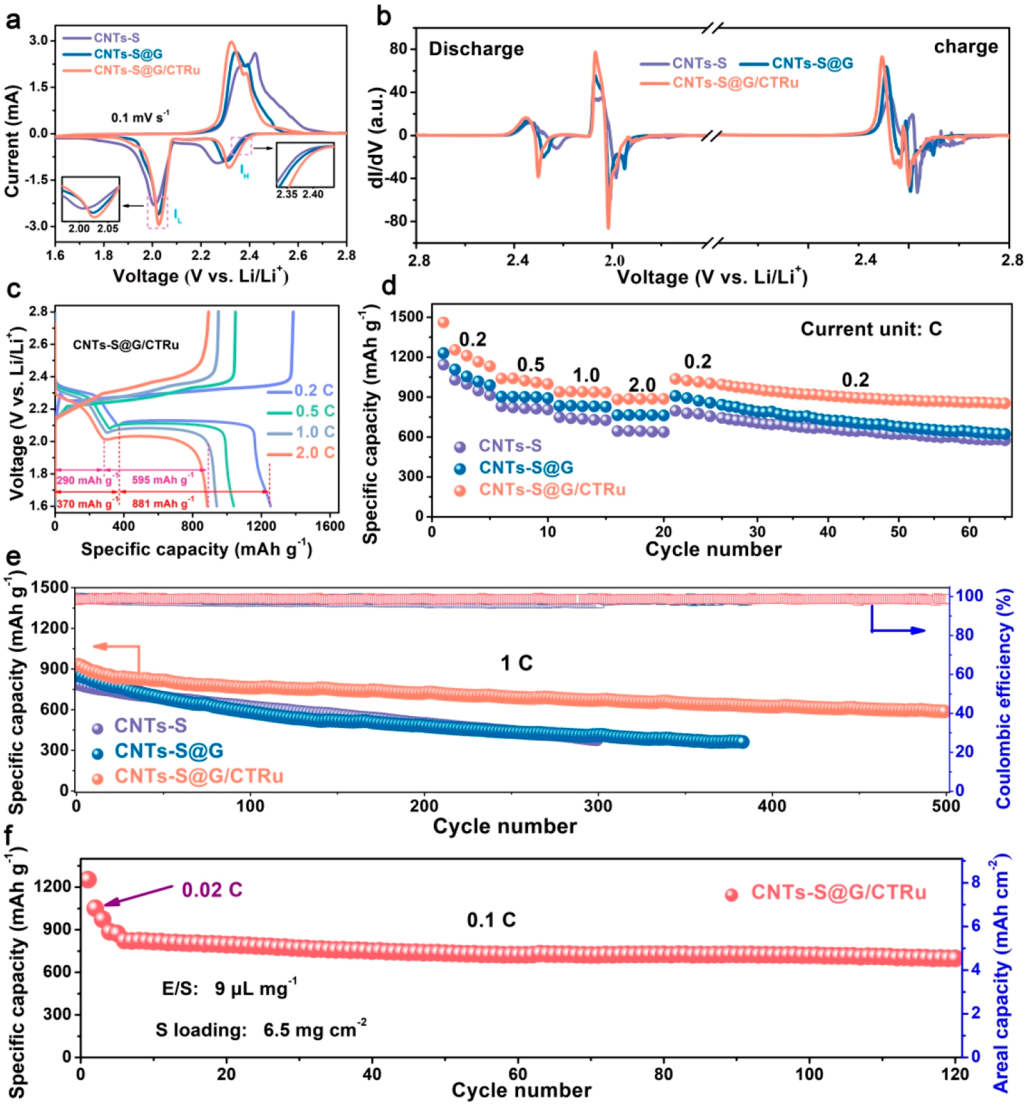

Figure 2. Electrochemical tests and performances of Li−S batteries with CNTs−S, CNTs−S@G, and CNTs−S@G/CTRu electrodes. (a) Steady state CV curves for the batteries with CNTs−S, CNTs−S@G, and CNTs−S@G/CTRu at a scanning rate of 0.1 mV s^{-1} and (b) their corresponding spectral derivative analysis. (c) Representative voltage-capacity profiles of CNTs−S@G/CTRu under 0.2, 0.5, 1, and 2 C. (d) Rate performances of CNTs−S, CNTs−S@G, and CNTs−S@G/CTRu electrodes under various current densities. (e) Long-term cycling performances of CNTs−S, CNTs−S@G, and CNTs−S@G/CTRu at 1 C. (f) Galvanostatic cycling performance of the thick CNTs−S@G/CTRu electrode (6.5 mg cm^{-2}) at 0.1 C under lean electrolyte (9 μL mg^{-1}).

together with two triphenylphosphine (PPh_3) functional groups and an axially coordinated Cl anion. After high-energy ultrasonic treatment, CTRu could be grafted onto highly active edge-defect sites of the G substrate, which resulted from acoustic streaming and cavitation caused by bubble formation, growth, vibration, and rupture (Figure S1 to 3). DFT calculations (Figure 1c) provided the optimized geometry of G/CTRu, in which P atoms of CTRu are chemically bonded with edge-defect sites of G. In addition, energy-dispersive spectroscopy (EDS) images obtained by scanning electron microscopy (SEM, Figure S2) and transmission electron microscopy (TEM, Figure S3) suggested massive and uniform dispersion of CTRu on the G films, as confirmed by variations in the nitrogen adsorption isotherms and specific surface areas (Figure S4). Owing to the anchoring effect, the solubility of G/CTRu in the electrolyte was significantly hindered, as indicated by the yellow color disappearing, in sharp contrast to the high solubility of pristine CTRu (Figure S5). Notably, this simple method helped to prevent the notorious dissolution of small organic molecules in Li−S electrolytes and contributed to their realization of homogeneous and heterogeneous catalysis.

To further demonstrate the effect of G/CTRu on LiPSs, their binding energies were evaluated by DFT simulations. As shown in Figure 1d and Figure S6, the optimized geometric configurations for the adsorption of Li_2S_8, Li_2S_6, Li_2S_4, Li_2S_2, and Li_2S gave binding energies of 1.73, 1.49, 1.37, 2.54, and 3.05 eV on G/CTRu and 1.02, 0.83, 0.93, 1.45, and 2.45 eV on G (Figure 1e), respectively. This indicated that coupling CTRu with the G film substantially enhanced the adsorption capability for LiPSs, mainly through Ru−S bonds, while retaining the three-dimensional G framework (Figure S3). Owing to the highly conductive and porous G substrate and high LiPS reactivity of CTRu, the shuttling of polysulfide anions can be prevented, without affecting electron/Li^+ transmission. Consequently, a coin cell with a sandwich structure comprising a G/CTRu interlayer and sulfur-

https://doi.org/10.1021/acsnano.2c00515
ACS Nano 2022, 16, 6414−6425

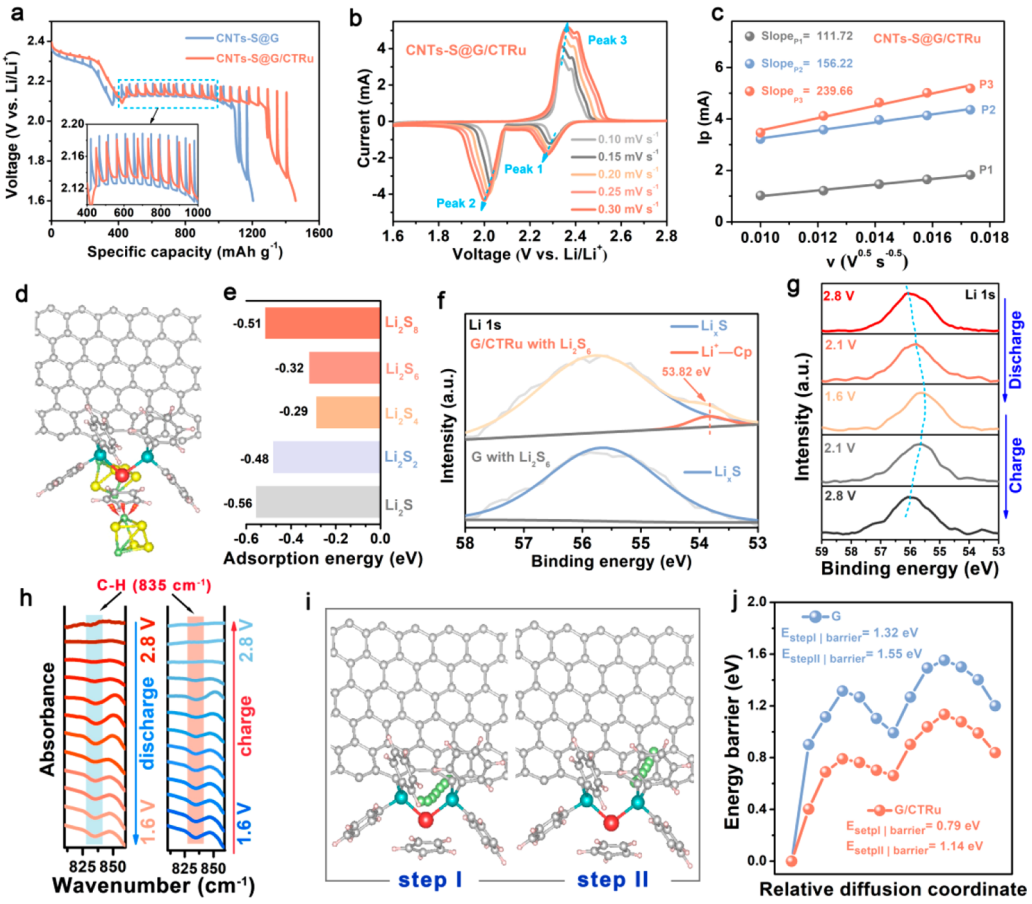

Figure 3. Transmission characteristics and mechanisms of Li^+ in G and G/CTRu interlayers. (a) GITT profiles of the Li−S cell with CNTs−S@G and CNTs−S@G/CTRu electrodes during the initial discharge at 0.05 C. (b, c) CV plots of CNTs−S@G/CTRu at various scanning rates and corresponding fitting curves at each redox peak (P1, P2, and P3 correspond to the first and second reduction peaks and the oxidation peak, respectively). (d) Representative optimized structure of another Li_2S_4 molecule adsorbed on the G/CTRu−Li_2S_4 substrate, where Li atoms in Li_2S_4 coupled with the electron-rich cyclopentadienyl (Cp) ring of CTRu. (e) Binding energies of Cp rings for Li_2S_8, Li_2S_6, Li_2S_4, Li_2S_2, and Li_2S. (f) Li 1s core levels of G/CTRu and G interlayers after soaking in Li_2S_6 solution. (g) High-resolution *ex-situ* Li 1s XPS spectra of the CNTs−S@G/CTRu electrode in a complete charge/discharge cycle. The cells ceased and disassembled at 2.8 (red), 2.1 (pink), and 1.6 V (light red) in the discharge process and 2.1 (light dark) and 2.8 V (dark) in the subsequent charge process. (h) *In situ* FTIR spectra of CNTs−S@G/CTRu electrode monitored in a CV voltage window of 1.6−2.8 V vs Li/Li^+, corresponding to the featured C−H vibration of the substituted Cp ring. The voltage difference between curves is set to 0.1 V. (i) Top views of Li atom migration routes on the G/CTRu interlayer which contains two steps (step I, from the adsorbed CTRu site to adjacent transition site; step II, from the transition site to bulk G). (j) Simulated Li atom diffusion energy barriers in the G/CTRu and G interlayers.

infiltrated carbon nanotube cathode (CNTs−S) was assembled, denoted as CNTs−S@G/CTRu (Figure 1d, left). Notably, the CTRu mass content of the CNTs−S@G/CTRu electrode was ~0.5 wt %. For comparison, electrodes with a G interlayer and without an interlayer were prepared, denoted as CNTs−S@G and CNTs−S, respectively. The sulfur content of the similar CNTs−S cathode was ~80.6 wt %, as determined using the thermogravimetric profile (Figure S7).

Superior Electrochemical Performance of Li−S Batteries with CNTs−S@G/CTRu Electrodes. To evaluate the electrochemical performance of the cell with a G/CTRu interlayer, a series of tests were conducted on the aforementioned coin cells with a sulfur loading of 1.2 mg cm^{-2}. Cyclic voltammetry (CV) measurements were performed after initial electrochemical activation (Figure 2a) at a scanning rate of 0.1 mV s^{-1}, and their spectral derivatives were analyzed, as shown in Figure 2b. In a voltage range of 1.6 to 2.8 V (vs Li/Li^+), the first (I_H, 2.31 V) and second (I_L, 2.03 V) reduction peaks corresponded to the conversion of S_8 to Li_2S_n ($4 \leq n \leq 8$) and then to Li_2S_2/Li_2S, respectively, while the oxidation peak (2.32 V) corresponded to the reversible formation of Li_2S_n and S_8. Comparatively, the CNTs−S@G/CTRu electrode exhibited the highest current densities at all three redox peaks, along with the earliest ascending/descending onset potentials upon discharging/charging (Figure 2b and insets of Figure 2a), indicating fast electrochemical reactions and noticeably improved kinetics using the G/CTRu interlayer. This was further confirmed by the smooth differential CV deformations and the smallest CV voltage hysteresis (~300 mV), compared with those of CNTs−S (~320 mV) and CNTs−S@G electrodes (~370 mV). Moreover, the calculated CV integrated current ratio of the high-to-low reduction region (I_H/I_L) was close to the theoretical value of 1:3 (Figure S8), confirming the boosting effect of G/CTRu on sulfur transformations. The exerted influence was stable and reversible, as suggested by the overlapping CV curves in subsequent cycles (Figure S9).

To measure the fast-charging properties, the voltage−capacity profiles (second cycle, Figure 2c and Figure S10) and specific discharge capacities (Figure 2d) of Li−S batteries

https://doi.org/10.1021/acsnano.2c00515
ACS Nano 2022, 16, 6414−6425

with CNTs−S, CNTs−S@G, and CNTs−S@G/CTRu electrodes were measured under various current densities. The CNTs−S@G/CTRu electrode delivered capacities of 1460, 1039, 938, and 881 mAh g^{-1} at rates of 0.2, 0.5, 1, and 2 C, respectively, which were much higher than those of CNTs−S (1173, 865, 778, and 676 mAh g^{-1}, respectively) and CNTs−S@G (1230, 902, 834, and 763 mAh g^{-1}, respectively). After returning the rate to 0.2 C, the discharge capacity of CNTs−S@G/CTRu recovered to 1035 mAh g^{-1} and showed the lowest decay (852 mAh g^{-1} after 65 cycles), exhibiting high reversibility and excellent rate performance. The improved performance compared with the control electrodes was attributed to the CTRu mediator activating sulfur species. By further adjusting the proportion of CTRu, a mass ratio of 1:5 in the G/CTRu interlayer was determined to be the optimal dosage of CTRu (Figure S11), probably due to a compromise between the high catalytic activity and relatively low conductivity of CTRu molecules. Unless otherwise specified, G/CTRu hereafter represents the optimal proportion of CTRu addition (1:5). The high catalytic activity of the CTRu mediator resulted in low-voltage polarization, as confirmed by the voltage difference of the charge and discharge platforms at 0.5 C (Figure S12), which was in the order of CNTs−S@G/CTRu < CNTs−S@G < CNTs−S. As a result, the long-term cycling test of CNTs−S@G/CTRu at 1 C (Figure 2e) delivered an initial discharge capacity of ∼932 mAh g^{-1} and maintained ∼587 mAh g^{-1} after 500 successive cycles, with a stable Coulombic efficiency of >98.5%. As shown in Figure 2f, even at a high sulfur areal loading of 6.5 mg cm^{-2} and an E/S ratio of 9 μL mg^{-1}, the thick CNTs−S@G/CTRu electrode still afforded a capacity of 698 mAh g^{-1} after 120 cycles with a mean decay rate of 0.13%. The combination of organic and inorganic components of CTRu can form a semi-immobilized structure on the electrode and may contribute to the solvation/desolvation of LiPSs and the affinities toward LiPSs,[31] providing a strategy to reduce the E/S ratio and develop high-energy Li−S batteries.

Exceptional Li^+ Transport Kinetics and Rapid Li^+ Supplements Enabled by the G/CTRu Interlayer. Elucidating the Li^+ migration routes and kinetics is essential because they largely determine the rate and capacity performances of Li−S batteries, especially during the conversion of short-chain LiPSs to solid Li_2S_2/Li_2S, when Li^+ supplementation faces multiple challenges. To gain insight into the overall effect of CTRu on Li^+ kinetics, the galvanostatic intermittent titration technique (GITT), which combines transient and steady-state measurements to eliminate interference from resistance polarization, was applied to determine the quasi-equilibrium reduction potentials (quasi-open circuit voltage, OCV) of Li−S batteries with CNTs−S@G and CNTs−S@G/CTRu electrodes (Figure 3a).[32] For CNTs−S@G/CTRu, the OCV was ∼45 mV higher than the non-equilibrium discharge voltage, and much lower than that of CNTs−S@G (∼62 mV; inset of Figure 3a), reflecting improved kinetics by the CTRu mediator. This effect was also verified using the chemical diffusion coefficient of Li^+ (D_{Li^+}) measured at various scanning rates by CV (Figure 3b and Figure S13).[33] On the basis of the Randles−Sevcik equation, a linear relationship between the peak current density and the square root of the scanning rate at each redox peak position suggested characteristics typical of ion diffusion-controlled reactions.[34] The calculated D_{Li^+} values for CNTs−S@G/CTRu at peaks P1, P2, and P3 were 1.74×10^{-8}, 3.40×10^{-8}, and 8.01×10^{-8} cm^2 s^{-1}, compared with 5.10×10^{-9}, 2.11×10^{-8}, and 2.08×10^{-8} cm^2 s^{-1} for CNTs−S@G, respectively, showing that the Li^+ diffusion rate was significantly enhanced by CTRu (Figure 3c and Figure S14).

Subsequently, DFT calculations combined with *in situ/ex situ* spectroscopic analysis were used to clarify the specific static/dynamic evolution mechanisms of Li^+ transfer. Figure 3d shows the representative adsorption configuration of another Li_2S_4 molecule adsorbed on the G/CTRu-Li_2S_4 substrate (Figure 1d). This indicated that the Cp ring was lithiophilic and able to adsorb additional Li_2S_8, Li_2S_6, Li_2S_4, Li_2S_2, and Li_2S with binding energies of 0.51, 0.32, 0.29, 0.48, and 0.56 eV, respectively (Figure 3e and Figure S15). Interestingly, post-mortem Li 1s X-ray photoelectron spectroscopy (XPS) tests after static adsorption with Li_2S_6 solution showed that a new peak emerged at ∼53.8 eV in G/CTRu compared with G (Figure 3f), which was attributed to the Li insertion behavior of the Cp ring through Li^+−Cp bond formation. To monitor the evolution of this phenomenon under electrochemical operating conditions, *ex situ* Li 1s XPS data were collected from batteries with CNTs−S@G and CNTs−S@G/CTRu electrodes ceasing and disassembling at various discharge/charge depths, as follows: fully charged state (2.8 V), half discharged state (2.3 V), fully discharged state (1.6 V), half charged state (2.3 V), and fully recharged state (2.8 V; Figure 3g). In stark contrast to the immovable peaks of CNTs−S@G (Figure S16), the initial Li 1s peak (∼56.1 eV) of CNTs−S@G/CTRu gradually shifted to a lower binding energy (∼55.6 eV) upon discharge, suggesting that Li atoms in LiPSs gained electron density during the reduction process and that strong electron transfer occurred from the anionic Cp ring to LiPSs.[35] In the subsequent charge process, the peak could reversibly return to its initial state (∼56.1 eV) when fully charged, implying reverse electron flow. Furthermore, *in situ* Fourier transform infrared (FTIR) spectroscopy was used to clarify the role of Cp sites. As shown in Figure 3h, the saturated C−H (∼835 cm^{-1}) peak originating from in-plane bending vibration was enhanced with discharge depths from 2.8 to 2.2 V and then remained stable until 1.6 V. Reversible evolution was observed in the subsequent charge process. In general, as the chain length of LiPSs (Li_2S_n, $3 \le n \le 8$) decreased, S atoms showed decreasing oxidizability and their bond lengths with counterpart Li^+ increased simultaneously (Table 1).[36,37] This indicated that Li atoms in long-chain LiPSs coordinated with Cp rings more readily. Therefore, with continuing discharge from 2.2 to 1.6 V, the generated soluble Li_2S_4 would finally be transformed into insoluble Li_2S_2/Li_2S and the residual soluble LiPSs would maintain an adsorbed state through Li−C_x bonds with the Cp rings. Put simply, the Cp ring in CTRu molecules donated/received electrons toward/from LiPSs through central C atoms.

Table 1. Bond Length of S−S and Li−S in LiPSs (Li_2S_n, $3 \le n \le 8$)[36,37]

Li_2S_n (n = 1−8)	Li−S bond length (Å)	S−S bond length (Å)
Li_2S_8	∼2.288	∼2.100
Li_2S_6	∼2.291	∼2.040
Li_2S_3	∼2.304	∼2.160
Li_2S_2	∼2.226	∼2.050
Li_2S	∼2.071	−

https://doi.org/10.1021/acsnano.2c00515
ACS Nano 2022, 16, 6414−6425

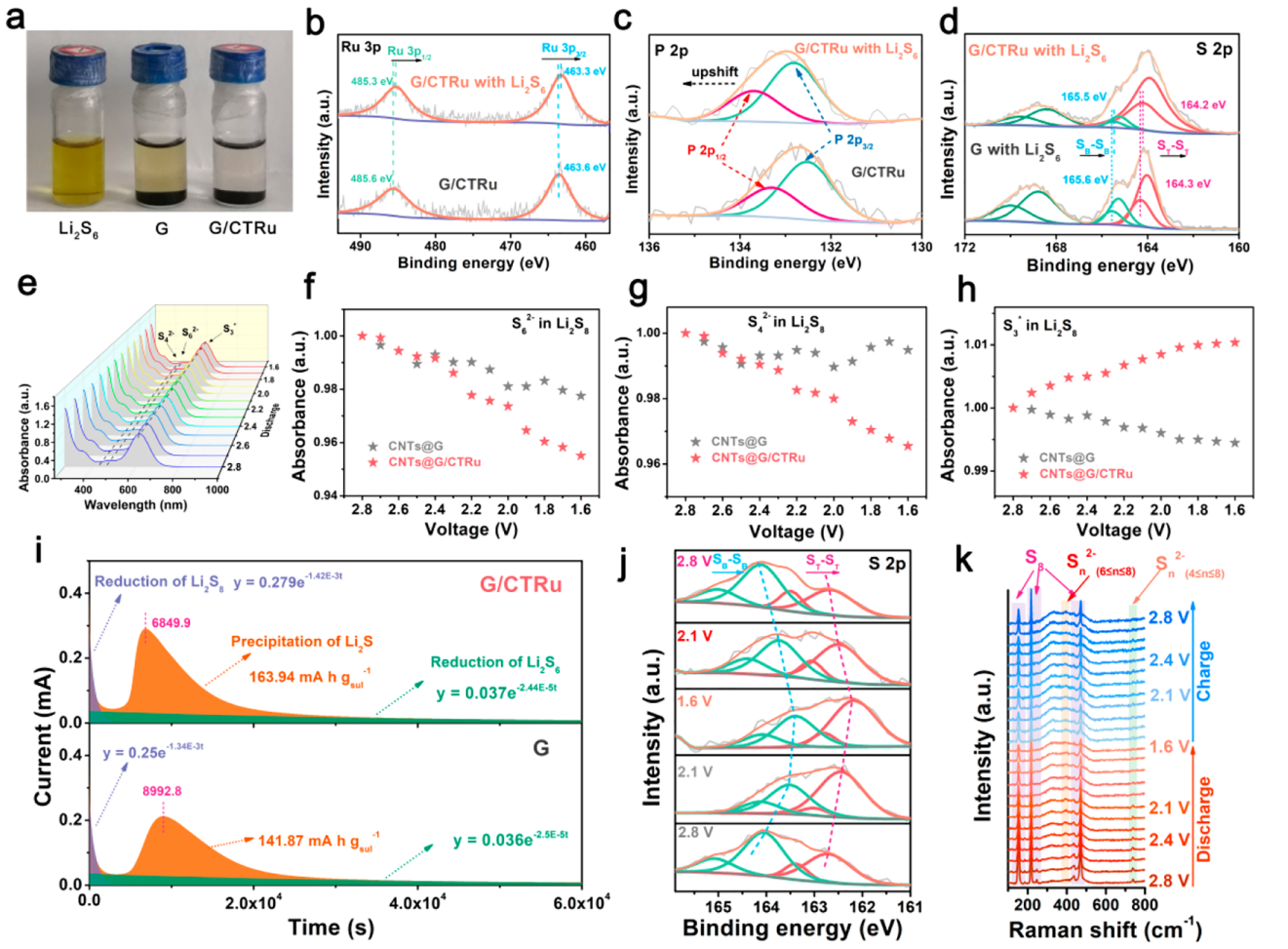

Figure 4. Insights into static/dynamic sulfur conversions in Li−S batteries with G and G/CTRu interlayers. (a) Digital photograph of Li_2S_6 solution after the addition of G and G/CTRu powders for 12 h. (b, c) P 2p and Ru 3p core levels of the G/CTRu interlayer before and after soaking in Li_2S_6 solution. (d) S 2p core levels of G/CTRu-Li_2S_6 and G-Li_2S_6. (e−h) *In situ* UV−vis spectroscopies and corresponding absorbance of S_6^{2-} (~475 nm), S_4^{2-} (~420 nm), and S_3^{*-} (~617 nm) in Li_2S_8 solution on CNTs−S@G and CNTs−S@G/CTRu electrodes during discharge. (i) Potentiostatic discharge profiles of Li−S batteries with CNTs−S@G/CTRu and CNTs−S@G electrodes at 2.04 V in a Li_2S_8 catholyte for evaluating Li_2S precipitation behaviors. (j) *Ex situ* high-resolution S 2p XPS spectra and (k) *in situ* Raman spectra of CNTs−S@G/CTRu electrode under various discharge/charge stages.

Considering both Li transfer contributions from the direct absorption of the lithiophilic Cp ring and indirect coordination of sulfiphilic Ru (Figure 3d) for LiPSs, migration paths of Li atoms on the surface of G/CTRu (Figure 3i) and G (Figure S17) models were established and compared using the climbing image nudged elastic band (CI-NEB) method. For the G interlayer, Li atoms were first located on edge-defect G sites and then migrated to the inner bulk with energy barriers of 1.32 and 1.55 eV (Figure 3j). In contrast, the migration in G/CTRu comprises two steps, as follows: (i) Li atoms migrate from the CTRu adsorption site to an adjacent transition site, and (ii) Li atoms migrate from the transition site to bulk G. The calculated energy barriers of these two steps were substantially lower than those of the G interlayer, at 0.79 and 1.14 eV, respectively (Figure 3j). These results confirmed that G/CTRu was favorable for reducing the energy barrier of Li atom diffusion and, therefore, enhancing the reaction kinetics of LiPSs.

Investigation of CTRu for Mediating Sulfur Conversions under Both Static and Dynamic Conditions. First, gas chromatography−mass spectrometry (GC−MS; Table S1) was conducted to confirm interactions between Li_2S_6 and CTRu molecules. After diluting with dimethyl sulfoxide (DMSO) as the solvent, the chromatographic retention times of CTRu in Li_2S_6 solution were 11.95 and 9.69 min, while those of Li_2S_6 and CTRu alone were 13.71 and 9.67 min, respectively, indicating a significant polarity change on CTRu molecules after treatment with Li_2S_6. As shown in the photograph of the static Li_2S_6 adsorption test (Figure 4a), the interaction between CTRu and Li_2S_6 was visualized, with the color of the Li_2S_6 solution fading with G/CTRu addition to a much greater extent than with G powder addition. Subsequently, XPS measurements were performed to analyze the compositions of the soaked G or G/CTRu surfaces.[38] Figure 4b shows the Ru 3p signals of G/CTRu with binding energies of 485.6 and 463.6 eV, which were assigned to Ru $3p_{1/2}$ and Ru $3p_{3/2}$, respectively. Upon adsorbing Li_2S_6, both peaks shifted to lower binding energies (485.2 and 462.3 eV), suggesting that Ru atoms in G/CTRu accepted electron density. In contrast, the characteristic P 2p XPS peaks (Figure 4c) shifted from 133.3 (P $2p_{1/2}$) and 132.5 eV (P $2p_{3/2}$) to higher values of 133.7 and 132.8 eV, respectively, indicating that P atoms lost electron density. This indicated that both Ru and P atoms from G/CTRu participated in the conversion of

https://doi.org/10.1021/acsnano.2c00515
ACS Nano 2022, 16, 6414−6425

LiPSs. Figure 4d shows the surface S 2p signals of G and G/CTRu after reacting with Li_2S_6 solution. The bridge (S_B) and terminal sulfur (S_T) signals for G were located at 165.6 and 164.3 eV, which shifted to 165.5 and 164.2 eV for G/CTRu, respectively. The decrease in binding energy suggested that electrons flowed from the coordinated CTRu molecules to Li_2S_6. Accordingly, the proportion of S_T in G/CTRu was greatly enhanced, emphasizing the interaction between CTRu and LiPSs. ^{31}P nuclear magnetic resonance (NMR) spectra, as shown in Figure S18, showed that P atoms definitely participated in the catalysis of LiPSs. The P−C bond (~27.25 ppm) in CTRu molecules was shifted slightly upfield to 27.48 ppm after treatment with prototype LiPS (Li_2S_6) solution with a weakened signal intensity, accompanied by a new strong peak emerging at 42.44 ppm, which suggested that the local coordination environment of P changed upon reaction with LiPSs. Notably, the P atoms influenced the catalysis of LiPSs through nondirect bond connections.

A more intuitive observation of the sulfur catalytic effect of CTRu was performed using potentiostatic experiments to evaluate the nucleation and growth of Li_2S on substrates.[39] Figure 4i shows the as-obtained Li_2S precipitation curves on the G/CTRu and G electrodes, with the starting electrolyte of Li_2S_8 and holding below the equilibrium potential (2.04 V).[40] The initial monotonically decreasing current was attributed to the depletion of remaining Li_2S_8 to Li_2S_4, and the subsequent regime was represented by a current peak owing to nucleation of Li_2S and its subsequent growth, whereupon the reaction practically ceased.[41] Li_2S nucleation was much more responsive on G/CTRu (6849.9 s) than on the G electrode (8992.8 s). Meanwhile, the calculated discharge capacity by Li_2S precipitation on G/CTRu was 163.9 mAh g^{-1} compared with 141.9 mAh g^{-1} on G, indicating a more thorough liquid−solid transformation of sulfur species. Figure S19a,b show the SEM morphologies of G/CTRu and G electrodes after the nucleation of Li_2S tests. Obviously, the G/CTRu electrode exhibits smaller particles and more uniform Li_2S depositions, as compared to that on the G substrate. The liquid-phase polysulfide conversion was also checked using symmetric CV measurements (Figure S20). The results showed that the electrodes using G/CTRu exhibited higher current densities than those using G under the same conditions, highlighting the role of CTRu in enhancing the liquid−liquid redox kinetics.[41,42] Electrochemical impedance spectroscopy (EIS) further confirmed the above deductions. Figure S21a−f show the Nyquist and fitting curves of Li−S cells with CNTs−S@G and CNTs−S@G/CTRu electrodes after 10, 50, and 100 cycles. The electrolyte (R_e, ~13.7 Ω), charge-transfer (R_{ct}, ~5.9 Ω), and mass-transfer (R_{mt}, ~4.4 Ω) resistances of CNTs−S@G/CTRu, corresponding to the ultrahigh-frequency intersection, high-frequency semicircle, and middle-frequency semicircle, decreased evidently to 6.2, 2.8, and 4.5 Ω, respectively, after 100 successive cycles. In stark contrast to CNTs−S@G, the significantly improved R_{ct} of CNTs−S@G/CTRu indicated fast electron/ion transfer behavior and effective promotion of LiPS conversions.

Subsequently, dynamic monitoring techniques were conducted to trace the features of sulfur evolution. Figure 4e shows typical *in situ* ultraviolet−visible (UV−vis) adsorption spectra of Li_2S_8 species on CNTs−S@G and CNTs−S@G/CTRu electrodes in various charge/discharge states. As the discharge depth increased, the normalized intensities of the absorbance peaks were recorded at ~475 (Figure 4f), ~420 (Figure 4g), and ~617 nm (Figure 4h), corresponding to the S_6^{2-}, S_4^{2-}, and S_3^{*-} anions, respectively.[43,44] The initial increase in intensity of S_6^{2-} and S_4^{2-} on CNTs−S@G/CTRu was attributed to the reduction of S_8^{2-} at a potential above 2.5 V and was followed by a drastic decrease. Impressively, the intensity of S_3^{*-} radicals on CNTs−S@G/CTRu increased as a function of potential below 2.1 V, showing a better catalytic capability to convert long-chain LiPSs to S_3^{*-} radicals achieved by introducing CTRu molecules. *Ex situ* XPS spectra were recorded to confirm the stability and reversibility of catalysis. Figure 4j and Figure S22 show the S 2p XPS evolutions of CNTs−S@G and CNTs−S@G/CTRu electrodes after ceasing and dissembling the cell at 2.8, 2.1, and 1.6 V during discharge and 2.1 and 2.8 V in the subsequent charge process. For the CNTs−S@G/CTRu electrode, the two pairs of fitted peaks attributed to S_B−S_B and S_T−S_T gradually shifted to higher binding energies at 2.8 V (~164.1/165.0 eV; ~162.7/163.5 eV) compared with 1.6 V (~163.4/164.1 eV; ~162.2/162.8 eV) in the reduction process, respectively, but recovered to their initial states (~164.1/165.1 eV and ~162.7/163.4 eV at 2.8 V) in the subsequent oxidation process. In contrast to the stationary peaks of the CNTs−S@G electrode, the variable and reversible S 2p peaks of the CNTs−S@G/CTRu electrode demonstrated that CTRu had different catalytic effects on different sulfur species and maintained stable catalysis under the cell operating conditions. *In situ* Raman spectra were measured to gain insight into the catalytic effect of CTRu on mitigating the shuttling of LiPSs. The potential-dependent peak intensities are shown in Figure 4k. In a complete discharge/charge cycle, the featured S_8 peaks (153.8, 217.1, and 417.8 cm^{-1}) of the CNTs−S@G/CTRu electrode first decreased and then increased, indicating reversible breaking and formation of cyclo-octasulfur. Meanwhile, the CNTs−S@G electrode experienced depletion of S_8 throughout the cycle and failed to return to its original state (Figure S23). Meanwhile, the peak (~738.5 cm^{-1}) of long-chain Li_2S_n ($4 \leq n \leq 8$) was hardly detected for CNTs−S@G/CTRu, in contrast to the obvious peak for CNTs−S@G, implying that CTRu retarded the dissolution of LiPSs.

PEC Concept: Using DFT Calculations to Clarify SRR Improvements through Ru−P Coordination. The results mentioned above demonstrate that both Ru and P atoms of CTRu participate in the SRR. To reveal their respective roles and determine the validity of our proposed PEC concept, the theoretical simulated atomic configurations of CTRu (RuP_2, catalytic center) and CTRu analogs were comparatively investigated by substituting metallic Ru and/or adjacent nonmetallic P atoms with Fe and/or N, respectively (denoted as FeP_2, RuN_2, and FeN_2). Figure 1c and Figure S24 show the optimized DFT models of these congeners after considering the rest of the compositions of the molecules. As shown in Table 2 and Figure S25, P substitution significantly increased certain bond angles, with P−(metal) M−P (~105.4° for RuP_2; ~109.5° for FeP_2) and M−P−C (~119.1° and 119.8° for RuP_2; ~121.2° and 121.9° for FeP_2) bond angles being larger than that of the corresponding N−M−N (~65.6° for RuN_2; ~68.7° for FeN_2) and M−N−C (~36.2° and 59.1° for RuN_2; ~35.5° and 58.5° for FeN_2) bonds. In addition, the P−C (~1.85 Å) bond length was longer than that of the N−C bond (~1.46 Å). These increased bond lengths and angles helped to eliminate the steric hindrance of long-chain LiPS adsorption by the catalysts. In comparison, the M−N system with large steric hindrance was incapable of accommodating LiPS species,

https://doi.org/10.1021/acsnano.2c00515
ACS Nano 2022, 16, 6414−6425

Table 2. Key Parameters of Bond Angles and Lengths of Simulated RuP_2, FeP_2, RuN_2, and FeN_2 Models from DFT Calculations

	bond	RuP_2	FeP_2	RuN_2	FeN_2
bond angle (deg)	N_1/P_1–Fe/Ru–N_2/P_2	105.36	109.52	65.58	68.67
	Fe/Ru–N_1/P_1–C	119.06	121.22	36.17	35.47
	Fe/Ru–N_2/P_2–C	119.81	121.93	59.13	58.47
bond length (Å)	Fe/Ru–N_1/P_1	2.36	2.30	3.16	3.04
	Fe/Ru–N_2/P_2	2.33	2.27	2.46	2.30
	N_1/P_1–C	1.85	1.84	1.47	1.47
	N_2/P_2–C	1.85	1.83	1.46	1.45

which strictly inhibited catalysis and might be more conducive to the oriented catalysis of small molecules, such as O_2. Notably, the symmetric M–N–C and M–N bonds of RuN_2 and FeN_2 present discordant bond angles and lengths, respectively, making them vulnerable to structural damage under electrochemical conditions. For RuP_2 and FeP_2, similar bond angles and lengths made the catalytic molecule robust and endurable.

Without modulation of nonmetallic elements, Fe compounds obviously exhibit higher adsorption activities. In the case of organic molecules with metal active sites, the coupling interaction of transition metal d orbitals and nonmetal p orbitals causes atomic energy level hybridization and substantially changes the adsorption–catalysis chemistry of a catalyst. Through comprehensive consideration of the interactions of metal and nonmetal elements, the energy gap (ΔE_{d-p}) of the d band and p band was examined, as shown in Figure 5b (bottom), and the calculated results were in the order of RuP_2 (3.21 eV) < FeP_2 (3.87 eV) < RuN_2 (4.73 eV) < FeN_2 (5.33 eV). Herein, the much lower p-band center of N-based compounds (−7.35/−7.33 eV) compared with P-based compounds (−5.69/−5.83 eV) induced more electron transfer to the metallic d orbitals and resulted in a shift in the d band away from the Fermi level.

In brief, as illustrated in Figure 5c,d, we provided insights into the dynamic evolution of the LiPS–RuP_2 (FeP_2, RuN_2, and FeN_2) configurations and identified the two main factors involved: steric hindrance and the ΔE_{d-p} energy gap. In SRR, LiPS accumulation forms a concentration gradient that drives its ingress into rationally designed catalytic systems, where-

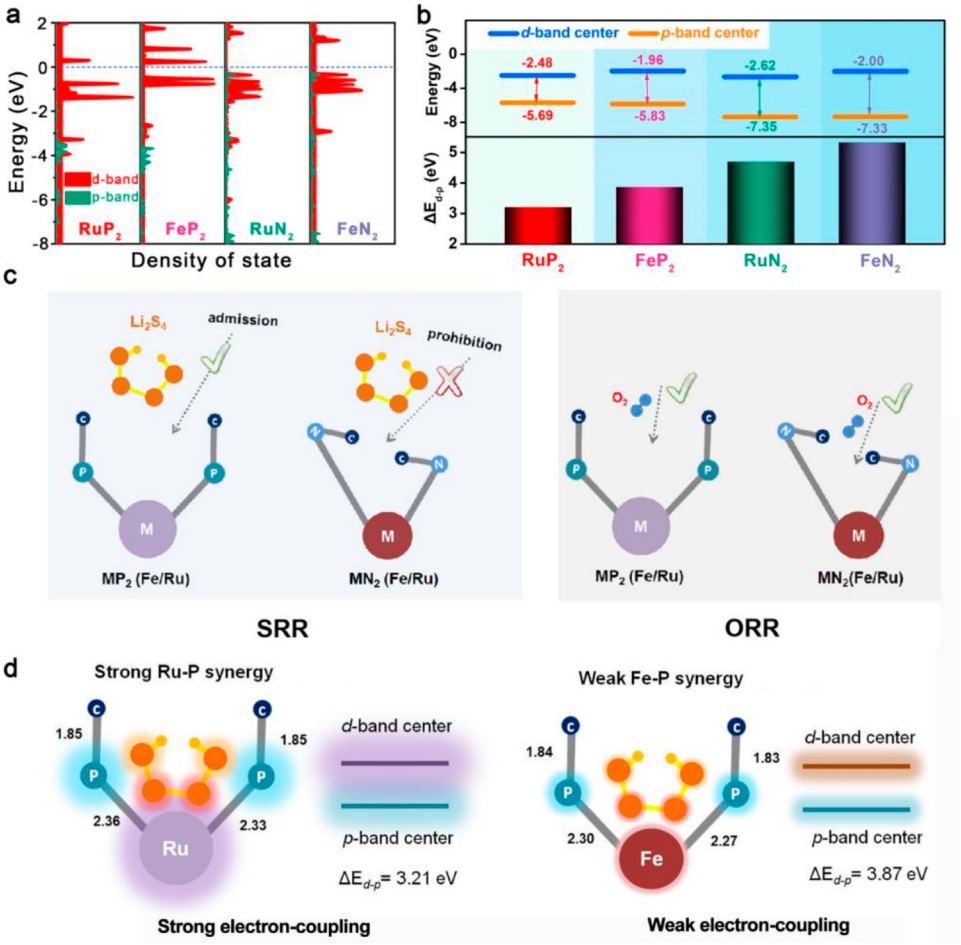

Figure 5. Unraveling the catalytic activity of CTRu through DFT calculations proposes a periodic expansion concept based on metal–nonmetallic synergistic effects. (a) Density of states analysis of the p and d bands of CTRu (RuP_2) and CTRu analogs by substituting its metal and localized coordination centers as FeP_2, RuN_2, and FeN_2. (b) Calculated metallic d bands and nonmetallic p bands of RuP_2, FeP_2, RuN_2, and FeN_2 (top) and the resultant d–p energy gap of ΔE_{d-p} (bottom). (c) Steric hindrance and stereoselectivity of RuP_2, FeP_2, RuN_2, and FeN_2 for adsorption of LiPSs (represented by Li_2S_4) and O_2, respectively, in the first step of ORR or SRR. (d) Stonger electron orbital couplings of P 2p with Ru 4d (RuP_2) than Fe 3d (FeP_2) that highlights the delocalization of π electrons from Ru to P for rapid transfer to LiPSs in the SRR catalysis.

https://doi.org/10.1021/acsnano.2c00515
ACS Nano 2022, 16, 6414–6425

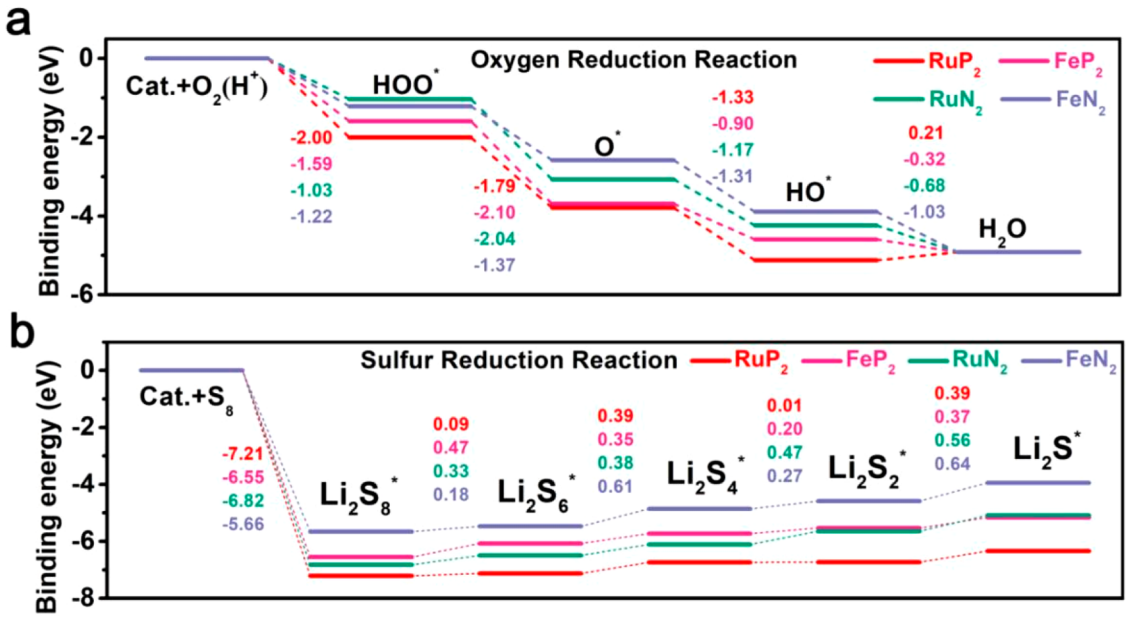

Figure 6. Gibbs free energy profiles for all intermediate states of the ORR or SRR using the four prototypes. (a) Free energy diagrams of 4e$^-$ pathways of the oxygen reduction reaction on the RuP_2 (red line), FeP_2 (magenta line), RuN_2 (cyan line), and FeN_2 (royal blue line) configuration surfaces. (b) Energy profiles for 2e$^-$ pathways of the reduction of Li_2S_n (n = 8, 6, 4, 2, 1) species on RuP_2, FeP_2, RuN_2, and FeN_2 congener substrates.

upon Li_2S_4, a representative LiPS species, would gain access in the first step to active RuP_2/FeP_2 sites, and that should not occur in RuN_2/FeN_2 systems due to a finite open space (Figure 5c). This indicates that large nonmetal atoms (P vs N) have a better ability to eliminate steric hindrance, which varies by the substrate (Li_2S_4 vs O_2). In the next step, the swallowed Li_2S_4 accepts or donates electrons from or to RuP_2/FeP_2. Comparatively, a small ΔE_{d-p} of RuP_2 (Figure 5b) implies strong orbital couplings of P 2p and Ru 4d, which means that electrons from Ru are prone to be delocalized and then extend outward from a single Ru atom to a P−Ru−P polyatomic system (Figure 5d). These delocalized electrons are more active and readily transferred to LiPSs, consequently improving the SRR kinetics. On the basis of the stereoselectivity and electronic structure analysis, FeN_2 was deduced to be more efficient for ORR catalysis, while RuP_2 was preferred for SRR catalysis, providing evidences of our proposed PEC concept.

The concept was further tested in specific ORRs and SRRs. Figure 6a shows the Gibbs free energy profiles for all intermediate states of the ORR using the four prototypes. The first ($O_2 + H^+ + e^- \rightarrow OOH^*$) or second electron transfer ($OOH^* + H^+ + e^- \rightarrow H_2O + O^*$) was the rate-determining step,[45,46] and the energy barriers for RuP_2, FeP_2, RuN_2, and FeN_2 were determined to be −2.00, −2.10, −2.04, and −1.37 eV, respectively. This suggested that FeN_2 had a superior catalytic effect on the ORR. Conversely, RuP_2 evidently increased the reaction difficulty of the first electron transfer and maintained a high reaction barrier for OOH* reduction (1.79 eV). The overall SRR reactions based on reversible formation of Li_2S from S_8 and Li bulk were also considered, as shown in Figure 6b.[47] The Gibbs free energy change (ΔG) from S_8 to Li_2S on the RuP_2 substrate (ΔG_{RuP2} = −6.33 eV) was more negative than that on the other three substrates (ΔG_{FeP2} = −5.16 eV; ΔG_{RuN2} = −5.08 eV; ΔG_{FeN2} = −3.96 eV), showing that SRR reduction was thermodynamically more favorable on RuP_2 during discharging. A positive ΔG for each stage of S_8 reduction is thermodynamically limiting, and the maximum ΔG step determines the reaction kinetics. The computational data indicated that RuP_2 possessed the lowest reduction barrier (0.39 eV), which was attributed to reactions of $Li_2S_6 \rightarrow Li_2S_4$ and $Li_2S_2 \rightarrow Li_2S$, followed by FeP_2 (0.47 eV), RuN_2 (0.56 eV), and FeN_2 (0.64 eV). Consequently, RuP_2 was proven to be thermodynamically and kinetically favorable for the SRR, in stark contrast to FeP_2, RuN_2, and FeN_2, which strongly validated our PEC concept.

CONCLUSIONS

This study proposed a concept, PEC, for precisely designing highly efficient SRR catalysts in Li−S batteries. To verify this concept, CTRu with a Ru/P complex was grafted onto edge-defect G substrates to form a G/CTRu interlayer, which facilitated LiPS adsorption, Li^+ diffusion, and catalytic conversion in the SRR. Furthermore, the respective roles of Ru and P atoms in the synergistic effect on the SRR were systematically investigated by DFT calculations. The elimination of steric hindrance and electronic regulation of the metal d band by coupling with the nonmetal p band were identified as fundamental reasons for the PEC of the SRR. Therefore, the rate performance and cyclic stability of Li−S batteries with a CNTs−S@G/CTRu electrode were substantially enhanced, even under high sulfur loading (6.5 mg cm^{-2}) and lean electrolyte (E/S = 9 μL mg^{-1}) conditions. The minimized dosage of the CTRu catalyst (~0.5 wt % of whole electrode) emphasized its efficient SRR promotion. This PEC concept of congener element couplings provides a basis for the precise screening of highly efficient catalysts in the field of advanced energy storage, including lithium/sodium/magnesium−oxygen/sulfur/selenium batteries and related scenarios, such as synthetic ammonia and carbon dioxide reduction.

https://doi.org/10.1021/acsnano.2c00515
ACS Nano 2022, 16, 6414−6425

EXPERIMENTAL SECTION

Synthesis of CNTs−S Cathode. A CNTs−S cathode was prepared via a conventional melting−diffusion treatment. Sulfur powder (>99.99%, metal basis, Aladdin) and commercial multiwalled CNTs (>95%, inner diameter: 3−5 nm, Aladdin) were fully ground at a mass ratio of 0.85:0.15 before being added to an enclosed bottle with appropriate carbon disulfide (CS_2, > 99.9%, Aladdin) solvent. The solution was then dried at 155 °C for 12 h. Thereafter, 85 wt % CNTs−S powder together with 5 wt % polyvinylidene fluoride (PVDF) and 10 wt % CNT conductive additive were uniformly dispersed in *N*-methylpyrrolidone (NMP) solution and stirred for 4 h. The slurry was coated on aluminum foil and evaporated at 55 °C in a vacuum oven for 8 h. The obtained film was punched into disks with a diameter of 12 mm. Unless otherwise stated, the sulfur loading on cathodes is ∼1.2 mg cm^{-2}.

Synthesis of CNTs−S@G and CNTs−S@G/CTRu Electrodes. CTRu (>98%, Aladdin) and commercial graphene (diameter, 0.5−5 μm; thickness, ∼0.8 nm; XFNano) with a weight ratio of 1:5 were dissolved in 2 mL of NMP solution. With a simple strategy of vigorous stirring and high-energy ultrasonic treatment, a homogeneous G/CTRu slurry was obtained and then coated on CNTs−S cathodes using a doctor blade. The obtained CNTs−S@G/CTRu electrode was then subjected to successive drying in a vacuum oven. For the CNTs−S@G electrode, no CTRu was added to the initial reactants. The interlayer thickness is adjustable by controlling the blade height.

Cell Assembly and Electrochemical Measurements. As mentioned above, the CR-2025 type coin cell with a CNTs−S, CNTs−S@G, or CNTs−S@G/CTRu electrode; a Celgard 2400 membrane separator; and a Li foil anode together with a moderate electrolyte (1 M lithium bis(trifluoromethanesulfonyl)imide (LiTFSI) and 1 wt % $LiNO_3$ in 1,3-dioxolane (DOL) and 1,2-dimethoxy ethane (DME) (1:1 v/v)) was assembled in an argon-filled glovebox with a water and oxygen content below 0.1 ppm. Unless noted, the electrolyte/sulfur ratio (E/S) was controlled to be ∼15:1 (μL mg^{-1}). A CHI 760E electrochemical workstation (Shanghai Chenhua, China) was used to conduct the CV, EIS, and Li_2S deposition tests. Specifically, the CV measurement was carried out in the voltage range of 1.6−2.8 V (vs Li/Li^+) with a scanning range from 0.1 to 0.3 mV s^{-1}. The EIS test was performed in the frequency range of 100 kHz to 0.01 Hz at open-circuit voltage with an AC amplitude of 5 mV. Galvanostatic charge/discharge data were collected from a Neware battery test system (Shenzhen Netware, China). In addition, all measurements were carried out at ambient temperature.

Material Characterization. XRD patterns were collected at room temperature from a D8 Advance powder diffractometer (Bruker, Germany) with Cu Kα radiation (40 kV, 40 mA, λ = 1.54 Å) at a speed of 10° min^{-1} and a step size of 0.025°. The JSM-6700F field emission scanning electron microscope and TECNAI G2F20 transmission electron microscope were used to observe the morphology and structure of various electrodes. The ^{31}P NMR spectra were recorded on a Bruker ARX500 spectroscope. XPS data were obtained by using an ultrahigh vacuum setup equipped with a monochromatic Al−K X-ray source (10 mA, 15 kV) and a high-resolution Gammadata-Scienta SES 2002 analyzer. The binding energy scale was calibrated to the C 1s peak (close to 284.8 eV), and the diameter of the analysis area was approximately 500 mm. To determine the surface chemical state of the electrode under cycling, the battery with a certain discharge/charge depth was disassembled in a glovebox and sealed in a vacuum bottle, which was quickly transferred to the XPS chamber (a basic pressure of 2×10^{-9} mbar) for *ex-situ* XPS measurements. ASAP 2020 M equipment was used to record nitrogen adsorption/desorption data at 77 K. Before the measurement, the sample was degassed at 200 °C for 4 h. The Brunauer Emmett Taylor (BET) equation was used to calculate the specific surface area. Thermogravimetry analyses (TGA, PerkinElmer, Diamond TG-DTA/Spectrum GX) were performed at a heating rate of 10 °C min^{-1} from 50 to 450 °C in an argon atmosphere to determine the actual sulfur content.

GITT Measurements. GITT was carried out on a CHI 760E electrochemical workstation within a potential range of 1.6−2.8 V (vs Li/Li^+) at room temperature. A current pulse of 0.05 C (84 mA g^{-1}) was kept for 20 min to measure the closed-circuit voltage and then turned off for 2 h to continuously obtain the quasi-open-circuit voltage. The first GITT curves of CNTs−S@G and CNTs−S@G/CTRu were recorded under quasi-equilibrium conditions.

Symmetric Cell Measurements. The symmetric cell was fabricated by using two identical G or G/CTRu sheets for working and counter electrodes with 50 μL of electrolyte (0.5 M of Li_2S_6 in DOL/DME (1:1 v/v)). The CV tests were performed at a speed of 10 mV s^{-1} in an applied voltage range of −0.5 to 0.5 V.

Nucleation of Li_2S. The as-assembled coin cell was first discharged to 2.06 V at a constant current of 0.112 mA. Thereafter, the chronoamperometric test was carried out at a constant potential of 2.04 V on a CHI 760E electrochemical workstation to obtain current−time curves. The deposition time was set as 1×10^5 s with a cutoff current of 1×10^{-5} A.

Visualized Adsorption of LiPSs. Li_2S_6 was selected as a representative long-chain LiPS, which was prepared by mixing Li_2S and sulfur powder at a molar ratio of 1:5 in DOL/DME (1:1, v/v) solution by intense stirring at 60 °C for 24 h. CTRu and G/CTRu of the same weight were added to 2.0 mL of Li_2S_6 solution (5.0 mM), and the static adsorption state was maintained for 12 h. Digital photographs were collected to evaluate the LiPS adsorptive capability of G and G/CTRu, and post-mortem XPS measurements were used to clarify the adsorption mechanisms.

DFT Calculations. Brillouin area sampling uses 2 × 2 × 1 single-peak packet grid k points for surface calculation, and double k-point grids are used to calculate the density of states (DOS). The hybrid system is modeled by a periodic two-dimensional graphene substrate with edge site CTRu molecules and LiPS adsorbates. The graphene surface is modeled by repeated periodic plates in 6 × 4 surface units, and the vacuum width between the plates along the *Z* axis is 30 Å. The adsorption energy of Li_2S_n ($1 \le n \le 8$) was calculated by $E_{ad} = E_{(G/CTRu)} + E_{(Li_2S_n)} - E_{(G/CTRu+Li_2S_n)}$ where $E_{(G/CTRu+Li_2S_n)}$ and $E_{(G/CTRu)}$ are the total energy of the surface with and without Li_2S_n ($1 \le n \le 8$) adsorbates $E_{(Li_2S_n)}$ is the free Li_2S_n ($1 \le n \le 8$) molecular energy. A positive E_{ad} value means that the corresponding adsorption structure is energetically favorable to form. The climbing image nudged elastic band (CI-NEB) method was used to confirm the transition states with only one imaginary frequency along the reaction coordinates.

***In Situ* FTIR/Raman Spectra.** *In situ* FTIR spectra were obtained on a Thermo Fisher iS50. First, the CNTs−S@G/CTRu slurry was coated on a carbon paper film. Then, carbon paper, Li sheets, and porous Celgard 2400 membranes were used as the cathode, anode, and separator, respectively, to assemble Li−S cells. To avoid strong absorption of the organic electrolyte, the cathode is closely attached to the triangular diamond window. According to the Lambert−Beer law, the attenuation of infrared light passing through a thin layer of electrolyte at an angle of 45° before reaching the electrode surface is estimated to be ∼0.3. Before collecting infrared data, the battery was charged and discharged for two cycles in the potential range of 1.6−2.8 V (vs Li/Li^+) with a sweep rate of 0.1 mV s^{-1}. Subsequently, the measurement was performed with an accumulation time of 10 s and recorded every 0.1 V. For the *in situ* Raman spectra, the same Li−S cell was assembled and tested at a scanning rate of 0.1 mV s^{-1}. For comparison, a Li−S cell with CNTs−S@G based cathode was tested under the same conditions.

***In Situ* UV−vis Spectra.** The Li_2S and S_8 powders were mixed in dimethyl sulfoxide (DMSO) solution at a stoichiometric ratio of 1:7 and stirred for 48 h to prepare a 0.5 mmol L^{-1} Li_2S_8 catholyte. Titanium wire and CNTs@G/CTRu modified glassy carbon electrodes were used as the counter and working electrodes, respectively. During the test, the sweep rate was set to 0.1 mV s^{-1} and the data were collected at a potential interval of 0.1 V. For comparison, the CNTs@G modified electrode was prepared by the same method.

https://doi.org/10.1021/acsnano.2c00515
ACS Nano 2022, 16, 6414−6425

ASSOCIATED CONTENT

Supporting Information

The Supporting Information is available free of charge at https://pubs.acs.org/doi/10.1021/acsnano.2c00515.

Additional experimental and characterization details related to SEM and TEM images; nitrogen sorption isotherms; solubility of G/CTRu in an electrolyte; optimized configurations of LiPSs on G/CTRu; TGA curves; CV profiles; galvanostatic charge−discharge profiles; rate performances; voltage profiles; diffusion coefficients of Li^+; *ex situ* S 2p XPS spectra; *ex situ* Li 1s XPS spectra; models of Li^+ migration routes; ^{31}P NMR spectra; SEM images of the Li_2S nucleation; CV measurements of symmetric cells; Nyquist plots; *in situ* Raman spectra; optimized configurations of CTRu analogs; gas chromatography spectrometry test (PDF)

AUTHOR INFORMATION

Corresponding Authors

Dong Cai − *Key Laboratory of Carbon Materials of Zhejiang Province, Wenzhou University, Wenzhou 325035, China*; Email: caidong@wzu.edu.cn

Zhi Yang − *Key Laboratory of Carbon Materials of Zhejiang Province, Wenzhou University, Wenzhou 325035, China*; orcid.org/0000-0002-9265-5041; Email: yang201079@126.com

Authors

Yangyang Dong − *Key Laboratory of Carbon Materials of Zhejiang Province, Wenzhou University, Wenzhou 325035, China*

Tingting Li − *Key Laboratory of Carbon Materials of Zhejiang Province, Wenzhou University, Wenzhou 325035, China*

Shuo Yang − *College of Electrical and Electronic Engineering, Wenzhou University, Wenzhou 325035, China*; orcid.org/0000-0001-8906-5289

Xuemei Zhou − *Key Laboratory of Carbon Materials of Zhejiang Province, Wenzhou University, Wenzhou 325035, China*

Yongjie Ge − *Key Laboratory of Carbon Materials of Zhejiang Province, Wenzhou University, Wenzhou 325035, China*

Hao Tang − *Key Laboratory of Carbon Materials of Zhejiang Province, Wenzhou University, Wenzhou 325035, China*; orcid.org/0000-0003-0323-0349

Huagui Nie − *Key Laboratory of Carbon Materials of Zhejiang Province, Wenzhou University, Wenzhou 325035, China*

Complete contact information is available at: https://pubs.acs.org/10.1021/acsnano.2c00515

Notes

The authors declare no competing financial interest.

ACKNOWLEDGMENTS

This research was funded by National Natural Science Foundation of China (Grant No. 22109119, 51972238, 22105147, and 21875166), Natural Science Foundation of Zhejiang Province (Grant No. LR18E020001 and LQ22B030003), Basic Scientific Research Projects of Wenzhou City (Grant No. G2020002 and H20210006), and Major Scientific and Technological Innovation Project of Wenzhou City (Grant No. ZG2021013).

REFERENCES

(1) Bhargav, A.; He, J.; Gupta, A.; Manthiram, A. Lithium-Sulfur Batteries: Attaining the Critical Metrics. *Joule* **2020**, *4*, 285−291.

(2) He, J.; Hartmann, G.; Lee, M.; Hwang, G. S.; Chen, Y.; Manthiram, A. Freestanding 1T MoS_2/graphene heterostructures as a highly efficient electrocatalyst for lithium polysulfides in Li−S batteries. *Energy Environ. Sci.* **2019**, *12*, 344−350.

(3) Zhao, M.; Li, B. Q.; Peng, H. J.; Yuan, H.; Wei, J. Y.; Huang, J. Q. Lithium-Sulfur Batteries under Lean Electrolyte Conditions: Challenges and Opportunities. *Angew. Chem., Int. Ed.* **2020**, *59*, 12636−12652.

(4) Zhou, S.; Yang, S.; Ding, X.; Lai, Y.; Nie, H.; Zhang, Y.; Chan, D.; Duan, H.; Huang, S.; Yang, Z. Dual-Regulation Strategy to Improve Anchoring and Conversion of Polysulfides in Lithium-Sulfur Batteries. *ACS Nano* **2020**, *14*, 7538−7551.

(5) Chu, H.; Noh, H.; Kim, Y. J.; Yuk, S.; Lee, J. H.; Lee, J.; Kwack, H.; Kim, Y.; Yang, D. K.; Kim, H. T. Achieving three-dimensional lithium sulfide growth in lithium-sulfur batteries using high-donor-number anions. *Nat. Commun.* **2019**, *10*, 188.

(6) Li, Y.; Wu, J.; Zhang, B.; Wang, W.; Zhang, G.; Seh, Z. W.; Zhang, N.; Sun, J.; Huang, L.; Jiang, J.; Zhou, J.; Sun, Y. Fast conversion and controlled deposition of lithium (poly)sulfides in lithium-sulfur batteries using high-loading cobalt single atoms. *Energy Storage Mater.* **2020**, *30*, 250−259.

(7) Wang, N.; Zhang, X.; Ju, Z.; Yu, X.; Wang, Y.; Du, Y.; Bai, Z.; Dou, S.; Yu, G. Thickness-independent scalable high-performance Li-S batteries with high areal sulfur loading via electron-enriched carbon framework. *Nat. Commun.* **2021**, *12*, 4519.

(8) Pei, F.; Lin, L.; Fu, A.; Mo, S.; Ou, D.; Fang, X.; Zheng, N. A Two-Dimensional Porous Carbon-Modified Separator for High-Energy-Density Li-S Batteries. *Joule* **2018**, *2*, 323−336.

(9) He, J.; Bhargav, A.; Yaghoobnejad Asl, H.; Chen, Y.; Manthiram, A. 1T′-ReS_2 Nanosheets In Situ Grown on Carbon Nanotubes as a Highly Efficient Polysulfide Electrocatalyst for Stable Li-S Batteries. *Adv. Energy Mater.* **2020**, *10*, 2001017.

(10) Wei, L.; Li, W.; Zhao, T.; Zhang, N.; Li, L.; Wu, F.; Chen, R. Cobalt nanoparticles shielded in N-doped carbon nanotubes for high areal capacity Li-S batteries. *Chem. Commun.* **2020**, *56*, 3007−3010.

(11) Xue, W.; Shi, Z.; Suo, L.; Wang, C.; Wang, Z.; Wang, H.; So, K. P.; Maurano, A.; Yu, D.; Chen, Y.; Qie, L.; Zhu, Z.; Xu, G.; Kong, J.; Li, J. Intercalation-conversion hybrid cathodes enabling Li-S full-cell architectures with jointly superior gravimetric and volumetric energy densities. *Nat. Energy* **2019**, *4*, 374−382.

(12) Song, Y.; Cai, W.; Kong, L.; Cai, J.; Zhang, Q.; Sun, J. Rationalizing Electrocatalysis of Li-S Chemistry by Mediator Design: Progress and Prospects. *Adv. Energy Mater.* **2020**, *10*, 1901075.

(13) Hu, A.; Chen, W.; Du, X.; Hu, Y.; Lei, T.; Wang, H.; Xue, L.; Li, Y.; Sun, H.; Yan, Y.; Long, J.; Shu, C.; Zhu, J.; Li, B.; Wang, X.; Xiong, J. An artificial hybrid interphase for an ultrahigh-rate and practical lithium metal anode. *Energy Environ. Sci.* **2021**, *14*, 4115−4124.

(14) Dong, Y.; Li, T.; Cai, D.; Yang, S.; Zhou, X.; Nie, H.; Yang, Z. Progress and Prospect of Organic Electrocatalysts in Lithium-Sulfur Batteries. *Front. Chem.* **2021**, *9*, 703354.

(15) Dörfler, S.; Althues, H.; Härtel, P.; Abendroth, T.; Schumm, B.; Kaskel, S. Challenges and Key Parameters of Lithium-Sulfur Batteries on Pouch Cell Level. *Joule* **2020**, *4*, 539−554.

(16) Ren, W.; Ma, W.; Zhang, S.; Tang, B. Recent advances in shuttle effect inhibition for lithium sulfur batteries. *Energy Storage Mater.* **2019**, *23*, 707−732.

(17) Chen, C. Y.; Peng, H. J.; Hou, T. Z.; Zhai, P. Y.; Li, B. Q.; Tang, C.; Zhu, W.; Huang, J. Q.; Zhang, Q. A Quinonoid-Imine-Enriched Nanostructured Polymer Mediator for Lithium-Sulfur Batteries. *Adv. Mater.* **2017**, *29*, 1606802.

(18) Ding, X.; Yang, S.; Zhou, S.; Zhan, Y.; Lai, Y.; Zhou, X.; Xu, X.; Nie, H.; Huang, S.; Yang, Z. Biomimetic Molecule Catalysts to

Promote the Conversion of Polysulfides for Advanced Lithium−Sulfur Batteries. *Adv. Funct. Mater.* **2020**, *30*, 2003354.
(19) Zhang, W.; Lai, W.; Cao, R. Energy-Related Small Molecule Activation Reactions: Oxygen Reduction and Hydrogen and Oxygen Evolution Reactions Catalyzed by Porphyrin- and Corrole-Based Systems. *Chem. Rev.* **2017**, *117*, 3717−3797.
(20) Li, Z.; Zhuang, Z.; Lv, F.; Zhu, H.; Zhou, L.; Luo, M.; Zhu, J.; Lang, Z.; Feng, S.; Chen, W.; Mai, L.; Guo, S. The Marriage of the FeN_4 Moiety and MXene Boosts Oxygen Reduction Catalysis: Fe 3d Electron Delocalization Matters. *Adv. Mater.* **2018**, *30*, 1803220.
(21) Zhu, Y.; Zhang, B.; Liu, X.; Wang, D. W.; Su, D. S. Unravelling the structure of electrocatalytically active Fe-N complexes in carbon for the oxygen reduction reaction. *Angew. Chem., Int. Ed.* **2014**, *53*, 10673−10677.
(22) Marshall-Roth, T.; Libretto, N. J.; Wrobel, A. T.; Anderton, K. J.; Pegis, M. L.; Ricke, N. D.; Voorhis, T. V.; Miller, J. T.; Surendranath, Y. A pyridinic Fe-N_4 macrocycle models the active sites in Fe/N-doped carbon electrocatalysts. *Nat. Commun.* **2020**, *11*, 5283.
(23) Hou, T. Z.; Xu, W. T.; Chen, X.; Peng, H. J.; Huang, J. Q.; Zhang, Q. Lithium Bond Chemistry in Lithium-Sulfur Batteries. *Angew. Chem., Int. Ed.* **2017**, *56*, 8178−8182.
(24) Park, K.; Cho, J. H.; Jang, J.-H.; Yu, B.-C.; De La Hoz, A. T.; Miller, K. M.; Ellison, C. J.; Goodenough, J. B. Trapping lithium polysulfides of a Li-S battery by forming lithium bonds in a polymer matrix. *Energy. Environ. Sci.* **2015**, *8*, 2389−2395.
(25) Cao, C.; Vernon, R. E.; Schwarz, W. H. E.; Li, J. Understanding Periodic and Non-periodic Chemistry in Periodic Tables. *Front. Chem.* **2021**, *8*, 813.
(26) Pan, H.; Chen, J.; Cao, R.; Murugesan, V.; Rajput, N. N.; Han, K. S.; Persson, K.; Estevez, L.; Engelhard, M. H.; Zhang, J.-G.; Mueller, K. T.; Cui, Y.; Shao, Y.; Liu, J. Non-encapsulation approach for high-performance Li-S batteries through controlled nucleation and growth. *Nat. Energy* **2017**, *2*, 813−820.
(27) Gao, Z.; Schwab, Y.; Zhang, Y.; Song, N.; Li, X. Ferromagnetic Nanoparticle−Assisted Polysulfide Trapping for Enhanced Lithium-Sulfur Batteries. *Adv. Funct. Mater.* **2018**, *28*, 1800563.
(28) Huang, S.; Huixiang, E.; Yang, Y.; Zhang, Y.; Ye, M.; Li, C. C. Transition metal phosphides: new generation cathode host/separator modifier for Li-S batteries. *J. Mater. Chem. A* **2021**, *9*, 7458−7480.
(29) Zhou, J.; Liu, X.; Zhu, L.; Zhou, J.; Guan, Y.; Chen, L.; Niu, S.; Cai, J.; Sun, D.; Zhu, Y.; Du, J.; Wang, G.; Qian, Y. Deciphering the Modulation Essence of p Bands in Co-Based Compounds on Li-S Chemistry. *Joule* **2018**, *2*, 2681−2693.
(30) Shen, J.; Xu, X.; Liu, J.; Wang, Z.; Zuo, S.; Liu, Z.; Zhang, D.; Liu, J.; Zhu, M. Unraveling the Catalytic Activity of Fe-Based Compounds toward Li_2S_x in Li-S Chemical System from d-p Bands. *Adv. Energy Mater.* **2021**, *11*, 2100673.
(31) Zhao, C.-X.; Li, X.-Y.; Zhao, M.; Chen, Z.-X.; Song, Y.-W.; Chen, W.-J.; Liu, J.-N.; Wang, B.; Zhang, X.-Q.; Chen, C.-M.; Li, B.-Q.; Huang, J.-Q.; Zhang, Q. Semi-immobilized molecular electrocatalysts for high-performance lithium−sulfur batteries. *J. Am. Chem. Soc.* **2021**, *143*, 19865−19872.
(32) Chen, J.; Zhang, H.; Yang, H.; Lei, J.; Naveed, A.; Yang, J.; Nuli, Y.; Wang, J. Towards practical Li-S battery with dense and flexible electrode containing lean electrolyte. *Energy Storage Mater.* **2020**, *27*, 307−315.
(33) Li, W.; Chen, K.; Xu, Q.; Li, X.; Zhang, Q.; Weng, J.; Xu, J. Mo_2C/C Hierarchical Double-Shelled Hollow Spheres as Sulfur Host for Advanced Li-S Batteries. *Angew. Chem., Int. Ed.* **2021**, *60*, 21512−21520.
(34) Zhao, M.; Chen, X.; Li, X.-Y.; Li, B.-Q.; Huang, J.-Q. An Organodiselenide Comediator to Facilitate Sulfur Redox Kinetics in Lithium−Sulfur Batteries. *Adv. Mater.* **2021**, *33*, 2007298.
(35) Mi, Y.; Liu, W.; Yang, K. R.; Jiang, J.; Fan, Q.; Weng, Z.; Zhong, Y.; Wu, Z.; Brudvig, G. W.; Batista, V. S.; Zhou, H.; Wang, H. Ferrocene-Promoted Long-Cycle Lithium-Sulfur Batteries. *Angew. Chem., Int. Ed.* **2016**, *55*, 14818−14822.
(36) Jayan, R.; Islam, M. M. First-Principles Investigation of the Anchoring Behavior of Pristine and Defect-Engineered Tungsten Disulfide for Lithium-Sulfur Batteries. *J. Phys. Chem. C* **2020**, *124*, 27323−27332.
(37) Yamsang, N.; Sittiwong, J.; Srifa, P.; Boekfa, B.; Sawangphruk, M.; Maihom, T.; Limtrakul, J. First-Principle study of lithium polysulfide adsorption on heteroatom doped graphitic carbon nitride for Lithium-Sulfur batteries. *Appl. Surf. Sci.* **2021**, *565*, 150378.
(38) Hong, X. J.; Song, C. L.; Yang, Y.; Tan, H. C.; Li, G. H.; Cai, Y. P.; Wang, H. Cerium Based Metal-Organic Frameworks as an Efficient Separator Coating Catalyzing the Conversion of Polysulfides for High Performance Lithium-Sulfur Batteries. *ACS Nano* **2019**, *13*, 1923−1931.
(39) Zhang, Y.; Liu, J.; Wang, J.; Zhao, Y.; Luo, D.; Yu, A.; Wang, X.; Chen, Z. Engineering oversaturated Fe-N_5 Multifunctional Catalytic Sites for Durable Lithium-Sulfur Batteries. *Angew. Chem., Int. Ed.* **2021**, *60*, 2−10.
(40) Zhao, M.; Li, B.-Q.; Chen, X.; Xie, J.; Yuan, H.; Huang, J.-Q. Redox comediation with organopolysulfides in working lithium-sulfur batteries. *Chem.* **2020**, *6*, 3297−3311.
(41) Fan, F. Y.; Carter, W. C.; Chiang, Y. M. Mechanism and Kinetics of Li_2S Precipitation in Lithium-Sulfur Batteries. *Adv. Mater.* **2015**, *27*, 5203−5209.
(42) Yuan, H.; Peng, H.-J.; Li, B.-Q.; Xie, J.; Kong, L.; Zhao, M.; Chen, X.; Huang, J.-Q.; Zhang, Q. Conductive and Catalytic Triple-Phase Interfaces Enabling Uniform Nucleation in High-Rate Lithium-Sulfur Batteries. *Adv. Energy Mater.* **2019**, *9*, 1802768.
(43) Chen, Y.; Zhang, H.; Xu, W.; Yang, X.; Yu, Y.; Li, X.; Zhang, H. Polysulfide Stabilization: A Pivotal Strategy to Achieve High Energy Density Li-S Batteries with Long Cycle Life. *Adv. Funct. Mater.* **2018**, *28*, 1704987.
(44) Hu, A.; Zhou, M.; Lei, T.; Hu, Y.; Du, X.; Gong, C.; Shu, C.; Long, J.; Zhu, J.; Chen, W.; Wang, X.; Xiong, J. Optimizing redox reactions in aprotic lithium-sulfur batteries. *Adv. Energy Mater.* **2020**, *10*, 2002180.
(45) Zhang, J.; Yang, H.; Liu, B. Coordination Engineering of Single-Atom Catalysts for the Oxygen Reduction Reaction: A Review. *Adv. Energy Mater.* **2021**, *11*, 2002473.
(46) Liu, Q.; Yu, B.; Liao, X.; Zhao, Y. Facet-Dependent Oxygen Reduction Reaction Activity on the Surfaces of Co_3O_4. *Energy Environ. Mater.* **2021**, *4*, 407−412.
(47) Sun, T.; Zhao, X.; Li, B.; Shu, H.; Luo, L.; Xia, W.; Chen, M.; Zeng, P.; Yang, X.; Gao, P.; Pei, Y.; Wang, X. $NiMoO_4$ Nanosheets Anchored on N-S Doped Carbon Clothes with Hierarchical Structure as a Bidirectional Catalyst toward Accelerating Polysulfides Conversion for Li-S Battery. *Adv. Funct. Mater.* **2021**, *31*, 2101285.

https://doi.org/10.1021/acsnano.2c00515
ACS Nano 2022, 16, 6414−6425